Annals of Anatomy 221 (2019) 125–134

Contents lists available at ScienceDirect

Annals of Anatomy

journal homepage: www.elsevier.com/locate/aanat

RESEARCH ARTICLE

Quantitative articular cartilage sub-surface defect assessment using optical coherence tomography: An *in-vitro* study

Roman Michalik[a,*], Thorn Pauer[b], Nicolai Brill[c], Matthias Knobe[d], Markus Tingart[a], Holger Jahr[e], Daniel Truhn[f], Sven Nebelung[f]

[a] Department of Orthopaedics, University Hospital Aachen, Aachen, Germany
[b] Fraunhofer Institute for Production Technology, Aachen, Germany
[c] Mabri Vision GmbH, Aachen, Germany
[d] Department of Orthopaedic Trauma, University Hospital Aachen, Aachen, Germany
[e] Institute of Anatomy and Cell Biology, University Hospital Aachen, Aachen, Germany
[f] Department of Diagnostic and Interventional Radiology, University Hospital Aachen, Aachen, Germany

ARTICLE INFO

Article history:
Received 9 November 2017
Received in revised form
20 September 2018
Accepted 1 October 2018

Keywords:
Optical coherence tomography
Osteoarthritis
Cartilage
Cartilage imaging
Sub-surface defect

ABSTRACT

Assessment of structural cartilage damage is of high scientific and clinical interest. Optical Coherence Tomography (OCT) is a light-based cross-sectional imaging modality that allows the real-time assessment of articular cartilage at near-histological resolution. Algorithm routines for the detection, parameterization and quantification of sub-surface defects as assessed by OCT were implemented and validated in this study.

Standard defects of 0.9 mm, 1.1 mm and 1.3 mm diameter were created in the sub-surface regions of macroscopically intact human articular cartilage samples (n = 60 defects of variable sizes in n = 20 samples). Subsequently, samples were scanned by 3D OCT and defect size, height, width and distance to the surface were determined based on the algorithm and related to manual measurements. Histology served as the standard-of-reference. Statistical analysis included one-way ANOVA's and Tukey's post-hoc test.

All defects were correctly identified by the algorithm, while five structural tissue inhomogeneities were erroneously marked as defects (sensitivity 100%, specificity: 92.3%). Inter-modality analysis revealed no significant differences in terms of defect area, height or width within the different defect sizes, while the distance to the surface was significantly different.

The comprehensive algorithm-based characterization of cartilage defects is consistent and reliable and allows their more objective evaluation. Given further research in this field, OCT and OCT-based quantitative measures may become clinically useful in the arthroscopic detection and evaluation of sub-surface cartilage defects.

1. Introduction

Loss of cartilage integrity can be caused by a variety of factors, among them degeneration and trauma. Articular cartilage damage to the knee is a common clinical problem (Cross et al., 2014; Hjelle et al., 2002; Johnson and Hunter, 2014; von Porat, 2004). Cartilage damage not only causes pain, but also predisposes to osteoarthritis (OA) (Felson and Zhang, 1998; Gelber et al., 2000; Messner and Maletius, 1996), a leading cause of disability in humans (Cross et al., 2014). Accurate diagnosis of early cartilage damage is necessary to prevent further degeneration and untreatable destruction of the joint. Because methods of therapeutic cartilage repair have improved over the past decade, scientific and clinical interest in detecting early cartilage changes has correspondingly increased (Winalski and Rajiah, 2011).

In clinical practice, conventional radiography is regularly used to detect structural bony changes and narrowing joint space width; yet, these changes are only indirect signs of OA and therefore, their sensitivity is low (Boegard et al., 1998; Kijowski et al., 2006).

Magnetic Resonance Imaging (MRI) is the imaging method of choice for the assessment of the entire joint; however, current literature indicates that MRI tends to underestimate cartilage defects (Campbell et al., 2013; Gomoll et al., 2011), while oftentimes not

* Corresponding author at: Department of Orthopaedics, University Hospital Aachen, Pauwelsstraße 30, Aachen 52074, Germany.
E-mail address: rmichalik@ukaachen.de (R. Michalik).

https://doi.org/10.1016/j.aanat.2018.10.001
0940-9602/

being readily available for financial and logistic reasons. To the knee surgeon, arthroscopy remains the gold standard of cartilage assessment because of direct visual inspection and tactile probing of the cartilage surface (de Bont et al., 2015; Nebelung et al., 2015; Oakley et al., 2005). However, it is only the cartilage surface that may be assessed by standard arthroscopy, while sub-surface changes cannot be evaluated. A number of studies have demonstrated that changes in the cartilage tissue, in particular following trauma, may not necessarily involve the cartilage surface and may remain unnoticed during arthroscopic evaluation (de Bont et al., 2015; Nebelung et al., 2015; Oakley et al., 2005; Szczodry et al., 2009). Cartilage traumatization can bring about cellular damage and extracellular matrix destruction while leaving the cartilage surface intact (Bear et al., 2010). If left undiagnosed and not comprehensively addressed therapeutically, these defects not only become symptomatic and severely affect the affected patients' quality of life (Heir et al., 2010) but also predispose the joint to further and accelerated degeneration (Ding et al., 2005).

Hence, a true clinical need exists for an adjunct diagnostic tool that may help assess sub-surface tissue areas of cartilage during arthroscopy. In consideration of the diagnostic gap outlined above, optical coherence tomography (OCT) is as an emergent diagnostic imaging modality that allows the assessment of surface and sub-surface areas of articular cartilage at near-histological resolutions (Chu et al., 2007, 2004, 2010; de Bont et al., 2015; Nebelung et al., 2015, 2014).

Based on the detection of near-infrared light, OCT delivers cross sectional images in real time without harmful interference with the tissue. Earlier *in-vitro* and *in-vivo* studies have demonstrated a close correspondence between OCT images and corresponding histological sections (Chu et al., 2010, 2007, 2004; de Bont et al., 2015; Nebelung et al., 2015, 2014). Cartilage samples have been assessed by OCT using bench-top systems as well as fibre-optic devices available during knee arthroscopy (Chu et al., 2004; Li et al., 2005; Xie et al., 2006). Further studies demonstrated the potential of assessing cartilage degeneration by OCT-based quantitative parameters like surface irregularity, tissue homogeneity and signal attenuation (Brill et al., 2015b; Nebelung et al., 2015, 2016). While surface changes have been systematically and thoroughly evaluated (Brill et al., 2015b, 2015a; Nebelung et al., 2016, 2014) sub-surface cartilage changes remain to be systematically parameterized and quantified.

Therefore, the aim of our study was to render the assessment of sub-surface cartilage changes more objectively, standardized and reliable by developing, validating and implementing dedicated algorithms for the comprehensive characterisation of sub-surface cartilage defects. By use of a standard defect model, the algorithm-based detection, parameterization and quantification of defect features in OCT datasets was evaluated and referenced to their corresponding manual characterization. Our hypothesis was that the defect detection and characterization by use of the algorithm would be similar to the manual defect characterisation regarding defect detection, size and distance to the surface.

2. Material and methods

2.1. Preparation of cartilage samples

Upon informed consent and approval by the Institutional Review Board (RWTH Aachen University, Germany, AZ-EK157/13) osteochondral samples from 10 patients (mean age 65.2 ± 6.0 years; 4 males, 6 females; 4 left knees, 6 right knees) were included in this study. All patients underwent total knee replacement surgery at our institution due to primary osteoarthritis of the knee. A detailed description of the preparation procedure

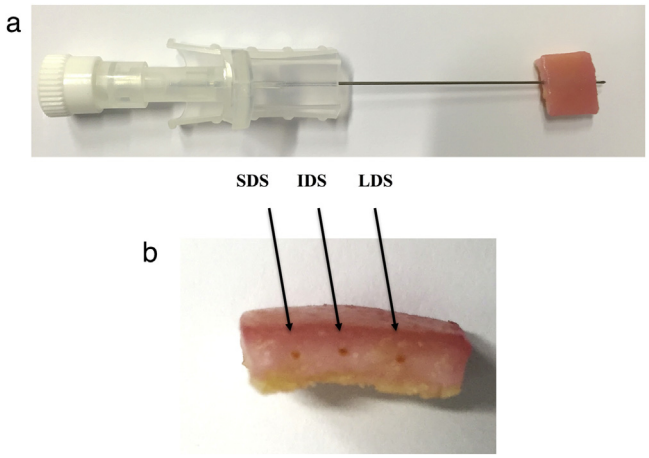

Fig. 1. Setup for standard sub-surface defect creation. Differently sized standard iv-catheter needles (a) were used to create horizontal defects parallel to the sample surface and the subchondral lamella at roughly 0.5–1 mm depth (b). After defect creation, every sample contained a cartilage defect of 0.9 mm diameter (SDS — small defect size), 1.1. mm diameter (IDS — intermediate defect size) and 1.3 mm (LDS — large defect size) as shown in (b). (For interpretation of the references to colour in the text, the reader is referred to the web version of this article.)

of the osteochondral samples has been reported before (de Bont et al., 2015; Nebelung et al., 2015, 2014). After surgical excision, cartilage-bone samples were placed in sterile DMEM medium (Gibco-BRL, Gaithersburg, USA) containing 100 U/mL penicillin (Gibco), 100 μg/mL gentamycin (Gibco), and 1.25 U/mL amphotericin B (Gibco). Samples were graded macroscopically using the Outerbridge classification (Outerbridge, 1961). Only samples from the lateral femoral condyle without signs of degeneration (*i.e.* Outerbridge grade 0) were included. Using dedicated surgical instruments (*i.e.* rongeur and saw), samples were cut to standard size of 20 × 20 mm (width × length), while the subchondral bone was trimmed to the subchondral lamella. Moreover, particular care was taken to create samples with their surface as plane as possible. For orientation purposes, small notches of 1 mm depth were created at opposing sample sides to mark the sagittal imaging plane, while a third notch perpendicular to the sagittal plane defined the orthogonal plane. Defects were created in line with the orthogonal plane, *i.e.* perpendicular to the sagittal plane (see below for details). Thirty samples were thus prepared and transferred to 12-well plates filled with 3 mL/well of DMEM + additives medium.

2.2. Standard sub-surface defect model

Each sample underwent standardized defect preparation. Using 22, 20 and 18 gauge needles of standard intravenous catheters (color codes: blue, pink and green; outer diameters 0.9 mm, 1.1 mm and 1.3 mm; Vasofix® Safety, B. Braun, Melsungen, Germany), one defect of each size, *i.e.* three defects in total, was created per sample (Fig. 1). The catheter needles were used to create sub-surface defects in a standardized manner: At a depth of ca. 1.0 mm below the sample surface and parallel to its surface contour longitudinal defects were created throughout the entire width of the sample. Particular care was taken to avoid stirring movements during defect creation as well as perforation of the surface. Samples were eliminated from the study if surface perforation occurred. Of the 30 samples initially prepared, 20 underwent complete standard sub-surface defect creation as outlined above, *i.e.* 10 samples had to be excluded because their surface was perforated (n = 7), the defect could not be created along the entire sample dimensions due to sample geometry (n = 2) or defect channels were converging due to cannula diversion (n = 1). Thus, in the 20 remaining samples, a total

of n = 60 differently sized sub-surface defects were created and distributed as follows: defect size 0.9 mm (small defect size — SDS), n = 20; defect size 1.1 mm (intermediate defect size — IDS), n = 20; defect size 1.3 mm (large defect size — LDS), n = 20.

2.3. OCT — setup and image acquisition

As in previous studies (de Bont et al., 2015; Nebelung et al., 2015, 2014), the acquisition of the OCT datasets was realized through a spectral-domain OCT device (Thorlabs, Dachau, Germany) with a superluminescent diode of 1325 nm wavelength, a bandwidth of 150 nm, an axial resolution of 7.5 μm in air and a lateral resolution of 17 μm (as measured in the focal plane).

The samples were aligned along the sagittal plane (*i.e.* in line with the 6-to-12 o'clock position) using a CMOS camera in line with the OCT beam. Prior to scanning, samples were cautiously dabbed using Kimwipes (laboratory tissue) to remove excess surface fluid. As before, OCT images were optimized in terms of focusing and artefact minimization (de Bont et al., 2015; Nebelung et al., 2015, 2014). 3D-OCT datasets were acquired with a field of view of $8 \times 8 \times 2.55$ mm (with a matrix of $512 \times 512 \times 512$ pixels), resulting in a numerical lateral spatial resolution of $15.6 \times 15.6 \times 4.98$ μm [length x width x depth]. A frequency of 28 kHz was used for A-scanning (*i.e.* obtaining the reflectivity profiles), thus a complete dataset was acquired within 11.6 s. One 3D-OCT-dataset (C-scan) consisted of 512 individual consecutive images (B-scans).

Of each sample, two 3D-OCT datasets were acquired within 10 min: The first dataset was obtained of the intact sample (prior to the creation of the standard defects), while the second dataset was obtained immediately after defect creation. Special care was taken to precisely align the samples in the same orientation during the subsequent dataset acquisitions.

2.4. OCT — data analysis and defect detection

The following paragraphs describe algorithmic details of the postprocessing of the acquired datasets. Sub-surface defects were detected, parameterized and quantified using dedicated algorithms, which can be principally separated into (a) the population of a database with image information, (b) the identification of regions-of-interest and detection of sub-surface defects, and (c) the quantitative characterization of detected defects.

The inevitable speckle noise was reduced by a multi-frame discrete stationary wavelet transformation with Haar wavelets based on the work of Mayer et al., (2012) which provides a precise distinction between tissue and noise. More specifically, the denoising process involved logarithmic transformation, wavelet decomposition, weight computing, coefficient weighting, averaging and wavelet reconstruction. Noise-optimized images were used to define the entire region-of-interest, *i.e.* the cartilage sub-surface cross-sectional area between the sample's surface contours and respective signal penetration depths. As published before (Brill et al., 2016), standard Canny edge algorithms, local regressive smoothing by application of weighted linear least squares and polynomial models were applied to detect the surface contours on an A-scan basis. Similarly, signal penetration depths were determined by detecting the last pixel above noise level for every A-scan. Algorithm-based defect detection was performed in a standardized manner by defining the defect's outlines within the region-of-interest. To this end, local signal minima and maxima were identified and subsequently parameterized in terms of signal intensity characteristics as a function of tissue depth (Fig. 2). Parameters of interest were (1) the slopes of respective maxima, (2) the distance of respective maxima, and (3) the difference of both maxima to the intermediate minimum. In pilot studies, the algorithm routines had been refined to increase the detection method's robustness as was required by variable surface conditions and residual speckle noise.

The theoretical background of the algorithm-based defect detection is displayed in more detail in Fig. 2. As sub-surface defects were characterized by hypoechogenic cores and hyperechogenic edges, signal intensity changes were considered to be indicative of defect outlines if two appropriate maxima and a respective intermediate minimum could be identified. In the following, $height_1$ and $height_2$ indicate the absolute heights of both maxima identified as peaks, $slope_1$ and $slope_2$ the ratio of the maxima's heights to their respective widths, max_1, max_2, min_1 and min_2 detected maxima and minima, $diff_1$ and $diff_2$ the signal intensity difference of each peak to its respective intermediate minimum with $diff_{max}$ being the signal intensity difference between both maxima, while *dist* indicates the required minimal depth-wise distance between both maxima.

For an illustration of the parameters please refer to Fig. 2. In the following, $y(max_i)$ and $x(max_i)$ are the signal intensity and depth of the i-th maximum, respectively, while the positions of the minima are determined accordingly. As a result of systematic evaluation, the following conditions (a–h) have been defined empirically:

$$condition\ a: slope_1 = \left|\frac{y(max_1) - y(min_1)}{x(max_1) - x(min_1)}\right| \geq 5$$

$$condition\ b: slope_2 = \left|\frac{y(max_2) - y(min_2)}{x(max_2) - x(min_2)}\right| \geq 5$$

$$condition\ c: diff_1 = y(max_1) - y(min_1) \geq 50$$

$$condition\ d: diff_2 = y(max_2) - y(min_2) \geq 50$$

$$condition\ e: dist = x(max_2) - x(max_1) \geq 10$$

$$condition\ f: diff_{max} = |y(max_1) - y(max_2)| < 30$$

$$condition\ g: |slope_1| < |2slope_2| \text{ if } |slope_1| > |slope_2|$$

$$condition\ h: |slope_2| < |2slope_1| \text{ if } |slope_2| > |slope_1|$$

A defect is identified if the following expression is true ($\vee$ for logical disjunctions; $\wedge$ for logical conjunctions):

$$defect = (a \wedge b \wedge c \wedge d \wedge e) \wedge (f \vee g)$$

Conditions a and b ensure that only suddenly occurring and sufficiently high changes in the signal intensity are considered as a potential peak. In a series of probatory tests different thresholds ranging from 1 to 15 with a step size of 0.1 for slope were systematically evaluated and the threshold value of 5 rendered slope definition most reliable. In future studies, this threshold value may have to be calibrated across different OCT systems and denoising algorithms to make defect detection results comparable between systems.

Conditions c and d ensure that maxima have a least difference of 50 in signal intensity values. This threshold value has been obtained in a similar manner as values <50 brought about higher false positive detection rates. A relative definition of the thresholds was also considered, though quickly discarded due to considerable image artifacts that rendered the application of relative thresholds (*e.g.* to the maximum value of 255) not feasible because of too numerous falsely detected peaks.

Condition e takes the distance between two detected peaks into consideration. If the depth-wise distance between two maxima was below the (again empirically determined) threshold value of 10, numerous peaks were considered as potential maxima and –

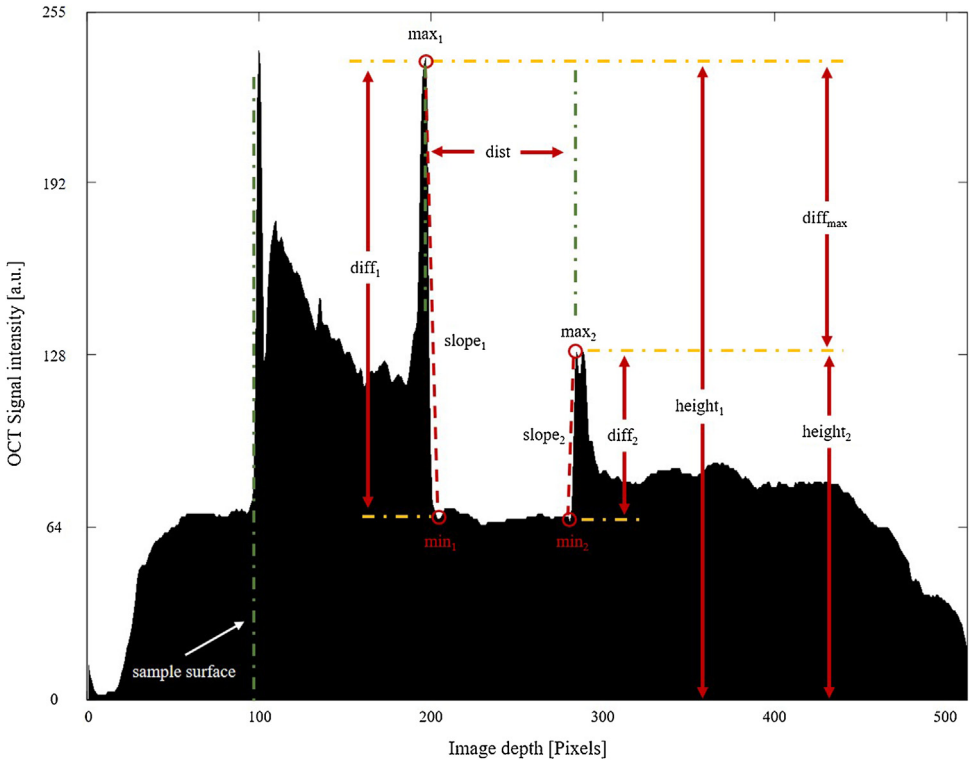

Fig. 2. OCT- and algorithm-based defect detection on an A-scan basis, *i.e.* as a function of tissue depth. Defect boundaries in the cartilage tissue were detected as alterations in signal intensity (y-axis, [arbitrary units]) along the tissue depth (x-axis, [pixels]). Here, two appropriate maxima and one intermediate minimum were sought to define the defect boundaries along the criteria (a–h) defined in the main text. See main text for an explanation of the terms and abbreviations.

consecutively – bounded areas as potential defects. Upon visual inspection these areas were determined as phantom defects, hence disregarded. The threshold value of 10 resulted in an acceptable rate of rejection of false positives while maximizing the correctly detected area of the defect.

Condition f limits the number of detected maxima pairs to allow for reliable defect boundary definition. To decrease user input, it was assumed that the signal intensities of the defect boundaries (in one OCT image) were comparably equal; hence, the y-values of the maxima were defined to be within the range of 30. This threshold value was again determined empirically and defined as 30.

Conditions g and h ascertain that both detected slopes are within a margin of 100%, which was again determined empirically to avoid erroneous pairings of two peaks of which one lies in close distance to the sample surface and the other close to the maximum penetration depth (with least signal intensity). In the context of image processing, "slope" is defined as a stark change in (OCT) signal intensity and roughly concordant with the basic definition of an edge which is defined as places in the image where there appears to be a jump in brightness value[s] or a local extremum in brightness value derivative[s] (Haralick, 1984). Due to the general decrease in signal intensity with increasing tissue depth, the signal intensity of the deeper maximum is usually lower, thereby necessitating this additional condition to be implemented.

Fig. 2 details the course of a single A-scan, *i.e.* the reflectivity profile (OCT signal intensities) along one thin parallel laser beam as a function of sample depth. For the algorithm-based defect detection, the following values for the conditions (a–g) may be calculated for this representative A-scan as follows:

a) $\left|\frac{238-67}{197-204}\right| = 24 \geq 5$

b) $\left|\frac{130-66}{285-281}\right| = 16 \geq 5$

c) $238 - 67 \geq 50$

d) $130 - 66 \geq 50$

e) $285 - 197 = 88 \geq 10$

f) $|238 - 130| = 108 > 30$

g) $24 < 2 \times 16 = 32$

The logical expression stated above can hence be filled as follows so that the detected area is considered a defect:

$$defect = (true \wedge true \wedge true \wedge true \wedge true) \wedge (false \vee true) = true$$

Any suggested defect was visually inspected and compared to the corresponding morphological B-scan OCT image. If the suggested defect equalled the visually detectable boundaries of a defect, the defect detection was considered correct.

Using this algorithm, the vertical edges of the defects were reliably and consistently defined; however, the algorithm required further refinement in the horizontal detection of defect boundaries because of decreasing signal intensities at the defect's edges.

To increase the algorithm's robustness and accuracy in the automatic defect detection, the processes of defect boundary definition and defect merging were performed sequentially. In a first optimisation step, each detected defect area was optimized in terms of its boundaries. The process started by identifying the border points of the currently detected defect (displayed in blue in Fig. 3a). From these border points, the centres of the nearest columns outside the current defect area were derived (displayed in yellow in

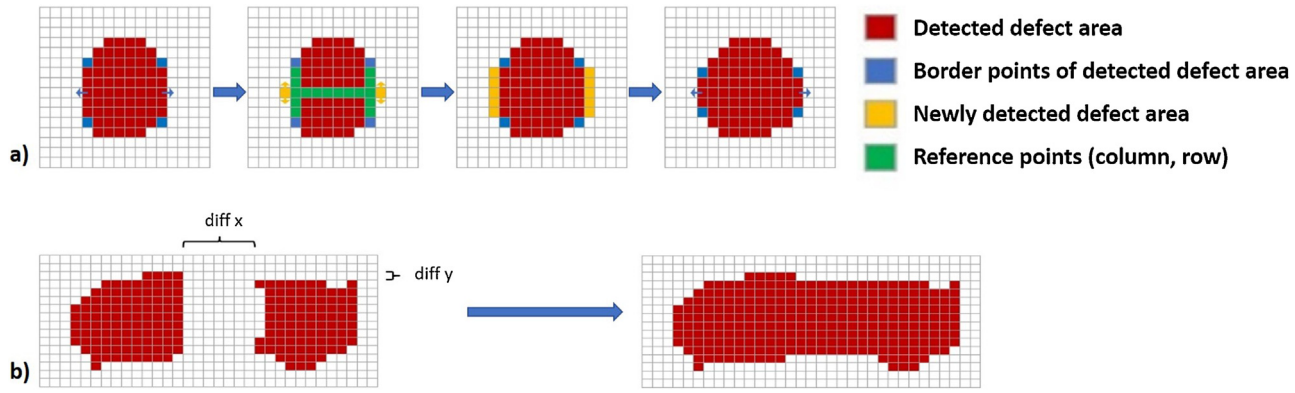

Fig. 3. (a) Schematic overview of the algorithm-based definition of defect boundaries. First, border points of the currently detected defect (displayed in blue) are identified that meet the conditions of a potential defect (a–h). Second, the centre of the nearest columns outside the current defect area are derived (displayed in yellow) and the new point's signal intensity is compared to the averaged signal intensities of the outermost column and central row of the currently detected defect area (displayed in green). If similar signal intensities of the new point and the references are determined, the new point is considered to be part of the defect area. Thereby, the algorithm moves onward and goes over the same process again. (b) Schematic overview of the algorithm-based merging procedure. Two neighbouring defect areas are merged if their respective distances in the x- and y-axis are below the threshold of 20 pixels (diff x ≤ 20 pixels; diff y ≤ 20 pixels). (For interpretation of the references to colour in this figure legend, the reader is referred to the web version of this article.)

Fig. 3a). The new point's signal intensity was then compared to the averaged signal intensities of the outermost column and central row of the currently detected defect area (displayed in green in Fig. 3a). If the suspected defect's signal intensity did not exceed 105% of the averaged column and row vectors, the point was considered to be part of the defect area due to similar signal intensities. Afterwards, the algorithm moved the point one pixel up- and downwards, respectively, and went over the same process again. The algorithm stopped automatically once no new points were detected that met the defect conditions (a–h) as detailed above. Following this optimization step, neighbouring defects were merged if specific requirements were met, *i.e.* the minimum differences in the x-axis and y-axis fell within the range of ≤20 pixels (Fig. 3b). This threshold had been determined empirically. Following the algorithm-based merging of two neighbouring defects, the resulting total defect area was considered as one defect and subsequently parameterized and quantified. Of note, the merging of neighbouring defects was performed automatically without user input or interaction.

Subsequently, algorithm-based defect boundary coordinates were checked for coherence. Coherent areas were only considered to constitute a defect if this area was ≥0.005 mm^2.

2.5. Sub-surface defect parameterization and quantification

Individual defects were parameterised and quantified in terms of defect area (DA), maximum defect width (DW), maximum defect height (DH) and the defect's distance to the surface (DS) using the above-mentioned algorithms. DA was determined by multiplying the total number of pixels (identified as belonging to the defect) with pixel size. On B-scans, the outermost left and right pixels of the defect area determined its maximum width (DW) [x-axis] and the outermost top and bottom pixels its maximum height (DH) [y-axis]. The distance to the surface was determined as the minimal distance of the outermost top of the defect to the surface contour on an A-scan basis [y-axis] (DS). Of note, each 3D-OCT dataset (C-scan) consisting of 512 images was automatically analysed using the algorithm as outlined above and identified defects were considered individually. Subsequent OCT data analysis including the algorithm-based detection, parameterization and quantification of the individual defects was performed within ca. 12 s per 2D-OCT image. Of note, the sagittal image, *i.e.* the 256th B-scan, was selected and analysed separately to allow for strict one image *vs.* one image comparisons with the manually determined OCT image and histological section. For reference purposes, the same defect characteristics (*i.e.* DA, DW, DH, DS) were manually determined on the sagittal OCT image (*i.e.* the 256th B-scan). To this end, ImageJ® software (National Institutes of Health, USA) was used to determine corresponding defect characteristics. Briefly, defect areas were identified and measured at their longest vertical and horizontal dimensions in height (DH) and width (DW) (in parallel with the x- and y-axis, respectively). DA was determined by manually delineating defect boundaries using the area calculation tool provided within ImageJ®. For the determination of DS, the smallest vertical distance of the defect outlines to the sample surface (in parallel with the y-axis) was used for subsequent analyses. One blinded observer (RM) performed the manual measurements. In the following, manually determined defect characteristics are referred to as OCT_m, while algorithm-based defect characteristics are referred to as OCT_a. Fig. 4 gives representative examples of manually determined defect characteristics.

2.6. Histological analysis

The histological analysis was performed as described previously (de Bont et al., 2015; Nebelung et al., 2015, 2014). Immediately following image acquisitions, samples were immersed in Ossa fixona (Diagonal, Muenster, Germany) for simultaneous decalcification and fixation. Once suitable for histological sectioning, samples were cut along the sagittal plane to 5-μm-thick sections that were subsequently stained with haematoxylin/eosin and Safranin O according to standard protocols. Sections were imaged using a light microscope (Leica DM/LM-P, Wetzlar, Germany) and documented using Diskus software (Leica). In analogy with the manual determination of defect characteristics on OCT images as outlined above, histological images were loaded into ImageJ® software and analysed by the same blinded observer (RM).

2.7. Statistical analysis

Statistical analysis was performed using GraphPad Prism Software (Version 7.0, San Diego, CA, USA). Upon confirmation of normality and equal variances, repeated measures ANOVA followed by Tukey's post-hoc test wherever appropriate was used to assess inter-modality differences. Of note, data from one sample constituted matched data rather than repeated measurements, which justified the selection of repeated measures ANOVA. P-values of $p \leq 0.05$ were considered significant, while levels of significance

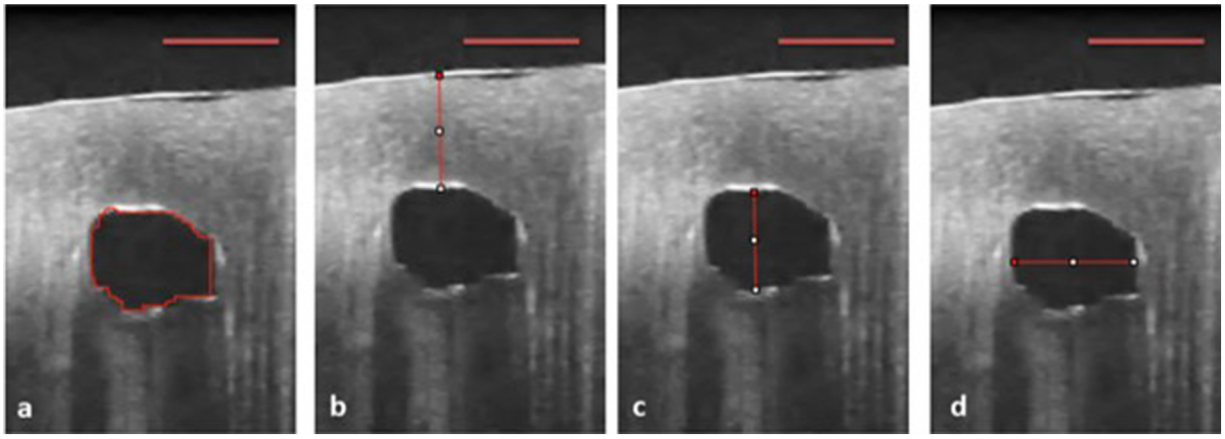

Fig. 4. OCT image example of manually determined defect characteristics: (intermediate defect) (a) the defect outlines (hypoechoic area) were delineated to determine the defect area (DA). (b) The distance to the surface (DS) was determined by measuring the shortest vertical distance from the defect area's top boundary to the sample surface. (c and d) maximum defect height (DH) and width (DW) were determined by measuring the defect's longest vertical and horizontal dimensions, respectively. Scale bars represent 500 μm.

were further classified as follows: [***] denotes $p \leq 0.001$, [**] $0.001 < p \leq 0.01$ and [*] $0.01 < p \leq 0.05$, while [ns] denotes no significant differences.

3. Results

In all samples the three differently sized sub-surface defects were visible macroscopically as well as clearly discernable in OCT images and in histological sections. In terms of sensitivity (true positive rate, *i.e.* TP/[TP + FN]), the algorithm detected all defects as such and did not miss any defect (60/[60 + 0] = 100%). However, in terms of specificity (true negative rate, *i.e.* TN/[TN + FP]), the algorithm marked five structures as defects that were later identified as signal inhomogeneities secondary to focal tissue alterations (60/[60 + 5] = 92.3%). These were identified as phantom defects due to their microscopic size and atypical form features. Examples are shown in Fig. 5.

Table 1 gives the quantitative characteristics of the detected sub-surface defects in relation to the measurement modality (*i.e.* OCT_a, OCT_m, histology) and the defect size (SDS, IDS, LDS). Overall, quantification revealed similar values for DA, DW, and DH, irrespective of the measurement modality and defect size. However, DS was consistently lower when measured on histological sections as compared to OCT images. Here, significant inter-group differences were found (SDS: p = 0.002; IDS: p = 0.005; LDS: p = 0.003), while post-hoc testing revealed these differences to be significant only between histology and OCT_m/OCT_a, while no significant differences were found between OCT_m and OCT_a.

Qualitative evaluation of defect morphology revealed slight intra- and inter-sample differences. The majority of defects had irregular and asymmetric configurations, while a minority of defects demonstrated distinct morphological patterns such as circularity, hemi-circularity or crescent shape. Defect morphologies were similar in OCT images and histological sections; Fig. 6 gives representative examples.

In OCT images the sub-surface defects were hypoechoic. Oftentimes, yet not consistently in all defects or samples, the defect edges were surrounded by a peripheral hyperechoic band that provided the transition to intact cartilage tissue. Histology revealed sharply defined borders in most defects. However, some defects, in particular those that were crescent-shaped, damaged edges were found in OCT images and corresponding histological sections.

4. Discussion

The most important findings of the present study are that the algorithm-based, user-independent assessment of sub-surface defects in human articular cartilage using a standardized defect model is consistent and reliable with the associated parameterization and quantification of defect features being closely related to manually determined defect features. In the orthopedic surgeon's clinical routine articular cartilage is commonly assessed by stand-alone arthroscopy. A survey conducted among experienced arthroscopic surgeons revealed that approximately half of them considered cartilage evaluation to be in need of improvement (Spahn et al., 2009). Nonetheless, evaluating subsurface defects and disruption is not possible by stand-alone arthroscopy. To depict sub-surface changes of the tissue structure, histological assessment is still the method of choice but not of clinical relevance due to its invasiveness. The sub-surface assessment is clinically highly relevant in post-trauma settings (Milentijevic et al., 2005; Thompson et al., 1991), where the coherent evaluation of the cartilage status in health and disease has direct therapeutic implications (Palmer et al., 2013).

In the present study, we demonstrated that sub-surface defects in cartilage could be reliably assessed using algorithm-based parameterization and quantification of defect characteristics in terms of defect area, height and width. Significant inter-modality differences, however, were found for the defect's mean distance to the sample surface between OCT and histology. Possible explanations involve the presence of restitution forces provided by the extracellular matrix upon defect creation. While OCT measurements were performed immediately after defect creation, full-scale histological fixation usually requires days to be completed, which could be a confounding factor. Moreover, besides a possible mismatch of the sagittal imaging planes, histological processing leads to considerable shrinkage of the tissue, which has been determined to account for a discrepancy of ca. 10% (Kladny et al., 1996). This aspect confounds our results and challenges the assessment of the algorithm's true accuracy.

In our experimental standardized defect model, we created defects of variable sizes to assess the algorithm's diagnostic potential. Even though significant needle-size related differences in the defect areas were found for histology and OCT, no significant inter-modality differences were determined for the different defect sizes, which is indicative of the algorithm's ability to detect defects of variable sizes, morphologies and configurations, thereby indicating

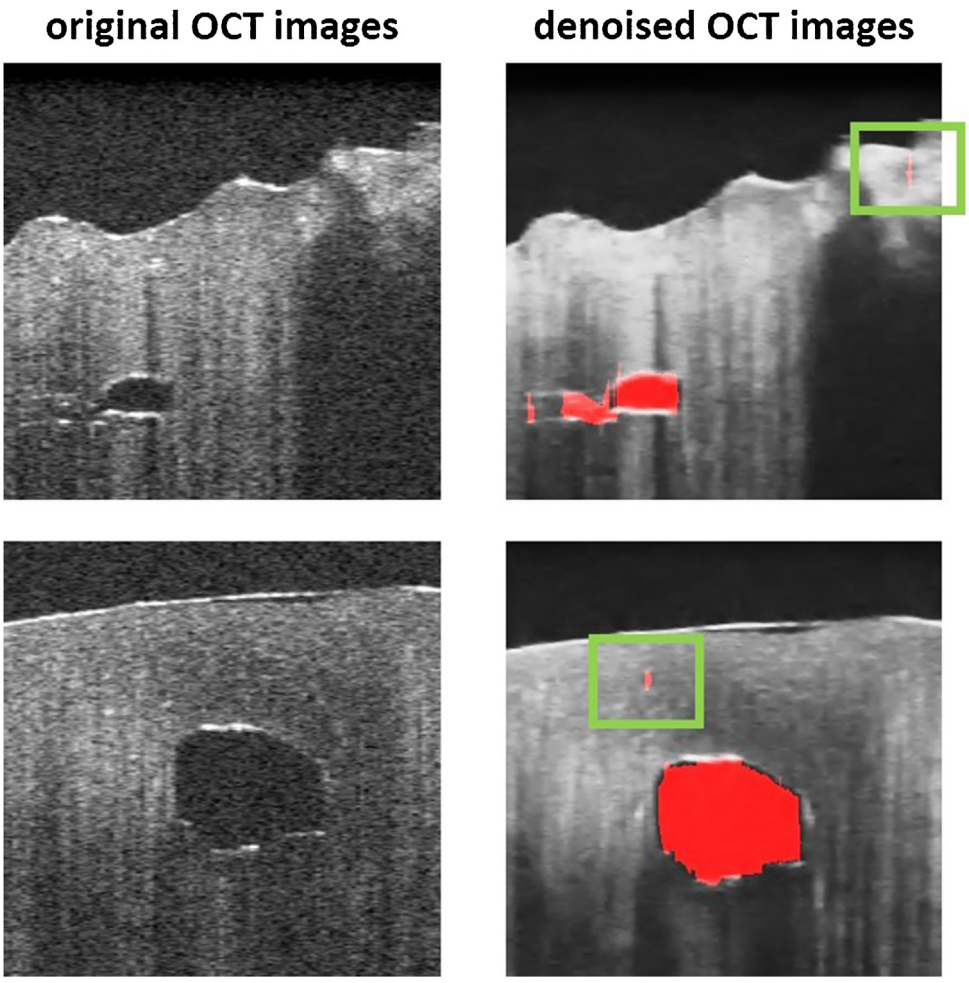

Fig. 5. Representative images to demonstrate the algorithm's performance in automatically detecting sub-surface defects that are outlined in red. Shown are the original (left) and denoised (right) OCT images. Phantom defects, *i.e.* tissue areas that have untruly been identified as constituting a defect, are surrounded by light green boxes, while correctly identified defects are not. (For interpretation of the references to colour in this figure legend, the reader is referred to the web version of this article.)

Table 1
Sub-surface defect characteristics as assessed by OCT and histology. Standardized sub-surface experimental defects of 0.9 mm, 1.1 mm and 1.3 mm outer diameter were created in human articular cartilage and assessed by OCT and histology. OCTa: algorithm-based quantification of defect characteristics based on all 512 OCT images; OCTm/histology: manual quantification of defect characteristics on OCT images/histological sections. Statistical assessment of inter-modality differences was performed by one-way ANOVA followed by Tukey's post-hoc tests. Significant differences are bold. Post-hoc testing revealed statistical significance only between histology and OCT-a/OCT-m. Needle size-related differences in the defect areas were significant for histology ($p = 0.007$ [**]) and OCTa ($p = 0.015$ [*]), while post-hoc testing revealed significant differences between SDS and LDS only.

	Small defect size (0.9 mm)				Intermediate defect size (1.1 mm)				Large defect size (1.3 mm)			
	OCT_a	OCT_m	Histology	P-value	OCT_a	OCT_m	Histology	P-value	OCT_a	OCT_m	Histology	P-value
Defect area [mm^2]	0.06 ± 0.04	0.08 ± 0.05	0.08 ± 0.06	P = 0.093	0.08 ± 0.03	0.10 ± 0.04	0.10 ± 0.07	P = 0.241	0.12 ± 0.11	0.12 ± 0.09	0.14 ± 0.08	P = 0.271
Defect height [mm]	0.36 ± 0.16	0.34 ± 0.15	0.43 ± 0.22	P = 0.149	0.41 ± 0.19	0.39 ± 0.15	0.42 ± 0.17	P = 0.608	0.44 ± 0.23	0.34 ± 0.16	0.43 ± 0.17	P = 0.174
Defect width [mm]	0.27 ± 0.11	0.36 ± 0.13	0.35 ± 0.15	P = 0.054	0.39 ± 0.16	0.46 ± 0,17	0.53 ± 0.23	P = 0.055	0.44 ± 0.19	0.53 ± 0.24	0.58 ± 0.24	P = 0.068
Distance to surface [mm]	0.92 ± 0.30	0.88 ± 0.31	0.64 ± 0.27	**P = 0.002**	0.75 ± 0.48	0.78 ± 0.44	0.53 ± 0.31	**P = 0.005**	0.96 ± 0.41	0.96 ± 0.36	0.74 ± 0.33	**P = 0.003**

its potential diagnostic utility and robustness. The algorithm identified and processed sub-surface defects with high sensitivity and specificity rates. Observers did not find additional defects as compared to the algorithm; however, a number of tissue irregularities were marked as defects, which decreased specificity. This is, most likely, the result of OCT image quality and needs to be controlled once the modality's *in-vivo* transfer is undertaken. Nonetheless, in consideration of clinical requirements and surgical workflows, the immediate identification, parameterization and quantification of sub-surface defects is a prerequisite for eventual clinical implementation. Therefore, close-to-real time quantitative evaluation, at least of single 2-D OCT images, was one of the present study's principal goals. Post-processing of the 3-D OCT datasets, which were acquired within ca. 12 s, could be started right away and allowed the nearly instantaneous quantitative evaluation of individual 2-D OCT images. However, as a result of the considerable and lengthy post-processing efforts required to evaluate the entire 3-D OCT dataset by means of the algorithm, the automatic full-sample evaluation is not yet practical to fit with surgical workflows. Once hardware capacities are further expanded and post-processing times thus shortened, the more timely analysis of entire 3-D OCT datasets may one day even be performed in a real-time manner.

Limitations of the study involve the defect model, as the standardized defects may be less challenging to detect and param-

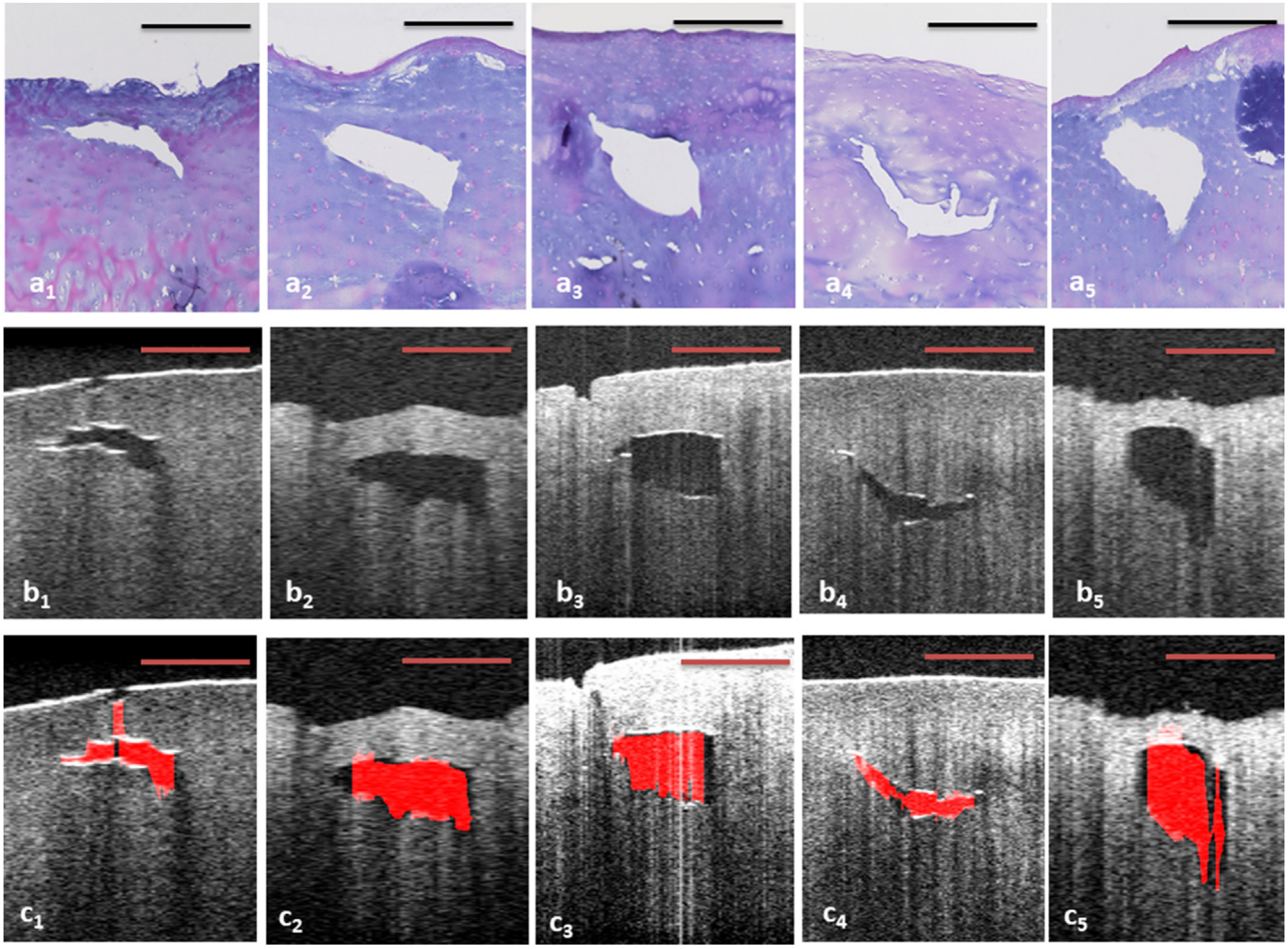

Fig. 6. Representative example images of standardized artificially created sub-surface defects in cartilage tissue ((a) histology; OCT images prior to (b) and after (c) processing using dedicated detection algorithm routines). Despite different morphologies, sub-surface defects that were clearly evident as intra-tissue substance defects in histological sections (a) had corresponding structural correlates (*i.e.* hypoechoic areas with well-delineated hyperechoic borders) on OCT images (b, c). Algorithm-based identification of defect outlines indicates substantial correspondence with the otherwise visible defect areas (red areas) (c). Scale bars represent 500 μm. (For interpretation of the references to colour in this figure legend, the reader is referred to the web version of this article.)

eterize by means of the algorithm than post-traumatic tissue changes encountered *in vivo*. Earlier studies demonstrated that traumatic impaction of human articular cartilage brings about horizontal lesions in the tissue's central parts (*i.e.* its mid-substance (de Bont et al., 2015) and along the entire tissue thickness (Verteramo and Seedhom, 2007). These lesions may be more complex to detect than the standardized defects created by needle stitching that are round and strong in contrast. Another aspect to consider is the *in-vitro* setting of this study: As OCT measurements were conducted in air, the sub-surface defects were filled with air, too, which is unlike the situation in the joint. It remains the work of future studies to carry the present experimental setup to a more physiological setting, *e.g.* by introducing fluid environments.

Further limitations that need to be overcome concern the algorithm's defect identification method in more degenerative cartilage tissue. As defect identification is principally based on the detection of structural alterations in signal intensity and transparency, partially inhomogeneous and less transparent tissue regions such as in more degenerated cartilage may not be as reliably assessed (Nebelung et al., 2014). In the present study, only coherently intact tissue regions (*i.e.* Outerbridge grade 0 samples) were included. As the samples were obtained from total knee replacements, the samples were therefore not reflective of the entire spectrum of degeneration, which in turn created standardized conditions for defect detection and characterization. Future studies assessing the algorithm-based characterization of sub-surface defects in cartilage should therefore include other methods of defect creation and more variably degenerated samples, which may be less transparent and thus more challenging to both algorithm and observers. Additionally, as far as reliability is concerned, rater bias cannot be entirely excluded because the manual defect characterisation on OCT images and histological sections was only performed by one author.

Another issue involves false-positive phantom defects, *i.e.* tissue areas that have been identified as a defect but in reality are not. These most likely arise due to limitations in the denoising process as a decent balance had to be found between preservation of real structure and noise level suppression. Inevitably, residual noise remained even in the denoised images that may have been falsely identified as defects. In the future, the level of false positives might be reduced by altering the algorithm's threshold for defect detection, however, this would come at the expense of lower sensitivities for the detection of real defects. Nonetheless, we found that false positives may be easily visually identified due to their microscopic size and atypical form features. Further limitations relate to the physical limitations of the OCT system used, which allows imaging of human cartilage to a depth of ca. 2.5 mm. As the average thickness of knee-joint cartilage covering the femur (2 mm), tibia (2.3 mm) and patella (3 mm) (Cohen, 1999) is possibly thicker than the modality's imaging depth, deeper located defects, *e.g.* delamina-

tions affecting the cartilage-bone transition, may therefore not be reliably assessed by OCT. Possible solutions involve modifications of the measurement setup (such as wavelength), as for example has recently been demonstrated for real-time terahertz imaging (Wade et al., 2016). Interestingly, the defects created by the differently sized catheter needles were quite irregular and asymmetric. Here, the dynamics of needle insertion forces, tissue deformation, needle deflection and variable trajectories as well as their bearing on tissue deformation have to be considered (thoroughly reviewed in Abolhassani et al., 2007). When the needle is inserted into the soft tissue, the tissue around the tip of the needle is compressed and the unbalanced resistance force against the compression deflects the needle. Moreover, bevel-tipped i.v. catheter needles such as the ones used in our study exert asymmetric forces so that cutting occurs at an offset angle. Due to the needle's grind, defects were cut rather than punched out and the flat grind of the needle tip favours sharpness over durability, which creates more focal tissue defects that are smaller than the needle's diameter. Hence, by their design, shape and sharpness these needles do not create a defect "hole" of consistent size and shape but rather irregularly shaped defects. In this context, another methodological limitation relates to the manual defect creation, which may have introduced inaccuracy. A potential way forward would be to use rigid fixtures and mechanical means to drive the needle into the tissue, *e.g.* by drill presses or punches, to create supposedly more standardized and symmetrical defects.

5. Conclusion

In conclusion, standardized sub-surface defects of human articular cartilage were systematically parameterized and quantified in this study. As referenced to histology, OCT-based algorithms for the automatic identification and quantification of these defects proved to be consistent and reliable. However, before implementing the algorithm into surgical workflows as a potential diagnostic tool, further research needs to be undertaken to further corroborate its diagnostic value in more complex configurations.

Author contribution statement

RM contributed to the data acquisition, interpretation, statistical analysis and writing of the manuscript. TP contributed to the data acquisition and the development of the algorithm. NB contributed to the development of the algorithm and data interpretation. MK, MT, HJ and DT contributed to data interpretation and the critical revision of the manuscript for important intellectual content. SN designed and oversaw the study, and contributed to data acquisition, interpretation, statistical analysis and writing of the manuscript. All authors read the final manuscript and agreed with its submission.

Acknowledgement

The authors would like to thank Ms. Sophie Lecouturier for her overall technical assistance.

Appendix A. Supplementary data

Supplementary data associated with this article can be found, in the online version, at https://doi.org/10.1016/j.aanat.2018.10.001.

References

Abolhassani, N., Patel, R., Moallem, M., 2007. Needle insertion into soft tissue: a survey. Med. Eng. Phys. 29, 413–431.

Bear, D.M., Szczodry, M., Kramer, S., Coyle, C.H., Smolinski, P., Chu, C.R., 2010. Optical coherence tomography detection of subclinical traumatic cartilage injury. J. Orthop. Trauma 24, 577–582, http://dx.doi.org/10.1097/BOT.0b013e3181f17a3b.

Boegard, T., Rudling, O., Petersson, I.F., Jonsson, K., 1998. Correlation between radiographically diagnosed osteophytes and magnetic resonance detected cartilage defects in the tibiofemoral joint. Ann. Rheum. Dis. 57, 401–407.

Brill, N., Riedel, J., Rath, B., Tingart, M., Jahr, H., Betsch, M., Quack, V., Pufe, T., Schmitt, R., Nebelung, S., 2015a. Optical coherence tomography-based parameterization and quantification of articular cartilage surface integrity. Biomed. Opt. Express 6, 2398, http://dx.doi.org/10.1364/BOE.6.002398.

Brill, N., Riedel, J., Schmitt, R., Tingart, M., Truhn, D., Pufe, T., Jahr, H., Nebelung, S., 2015b. 3D human cartilage surface characterization by optical coherence tomography. Phys. Med. Biol., 7747–7762, http://dx.doi.org/10.1088/0031-9155/60/19/7747.

Brill, N., Wirtz, M., Merhof, D., Tingart, M., Jahr, H., Truhn, D., Schmitt, R., Nebelung, S., 2016. Polarization-sensitive optical coherence tomography-based imaging, parameterization, and quantification of human cartilage degeneration. J. Biomed. Opt. 7, 076013, http://dx.doi.org/10.1117/1.JBO.21.7.076013.

Campbell, A.B., Knopp, M.V., Kolovich, G.P., Wei, W., Jia, G., Siston, R.A., Flanigan, D.C., 2013. Preoperative MRI underestimates articular cartilage defect size compared with findings at arthroscopic knee surgery. Am. J. Sports Med. 41, 590–595, http://dx.doi.org/10.1177/0363546512472044.

Chu, C.R., Izzo, N.J., Irrgang, J.J., Ferretti, M., Studer, R.K., 2007. Clinical diagnosis of potentially treatable early articular cartilage degeneration using optical coherence tomography. J. Biomed. Opt. 12, 051703, http://dx.doi.org/10.1117/1.2789674.

Chu, C.R., Lin, D., Geisler, J.L., Chu, C.T., Fu, F.H., Pan, Y., 2004. Arthroscopic microscopy of articular cartilage using optical coherence tomography. Am. J. Sports Med. 32, 699–709, http://dx.doi.org/10.1177/0363546503261736.

Chu, C.R., Williams, A., Tolliver, D., Kwoh, C.K., Bruno 3rd, S., Irrgang, J.J., 2010. Clinical optical coherence tomography of early articular cartilage degeneration in patients with degenerative meniscal tears. Arthritis Rheum. 62, 1412–1420, http://dx.doi.org/10.1002/art.27378.

Cohen, Z.A.E.A., 1999. Knee cartilage topography, thickness, and contact areas from MRI in-vitro calibration and in-vivo measurements. Osteoarthritis Cartilage, 1–15.

Cross, M., Smith, E., Hoy, D., Nolte, S., Ackerman, I., Fransen, M., Bridgett, L., Williams, S., Guillemin, F., Hill, C.L., Laslett, L.L., Jones, G., Cicuttini, F., Osborne, R., Vos, T., Buchbinder, R., Woolf, A., March, L., 2014. The global burden of hip and knee osteoarthritis: estimates from the Global Burden of Disease 2010 study. Ann. Rheum. Dis. 73, 1323–1330, http://dx.doi.org/10.1136/annrheumdis-2013-204763.

de Bont, F., Brill, N., Schmitt, R., Tingart, M., Rath, B., Pufe, T., Jahr, H., Nebelung, S., 2015. Evaluation of single-impact-induced cartilage degeneration by optical coherence tomography. BioMed Res. Int. 2015, 1–11, http://dx.doi.org/10.1007/s00167-010-1054-z.

Ding, C., Garnero, P., Cicuttini, F., Scott, F., Cooley, H., Jones, G., 2005. Knee cartilage defects: association with early radiographic osteoarthritis, decreased cartilage volume, increased joint surface area and type II collagen breakdown. Osteoarthritis Cartilage 13, 198–205, http://dx.doi.org/10.1016/j.joca.2004.11.007.

Felson, D.T., Zhang, Y., 1998. An update on the epidemiology of knee and hip osteoarthritis with a view to prevention. Arthritis Rheum. 41, 1343–1355, http://dx.doi.org/10.1002/1529-0131(199808)41:8<1343::AID-ART3>3.0.CO;2-9.

Gelber, A.C., Hochberg, M.C., Mead, L.A., Wang, N.Y., Wigley, F.M., Klag, M.J., 2000. Joint injury in young adults and risk for subsequent knee and hip osteoarthritis. Ann. Intern. Med. 133, 321–328.

Gomoll, A.H., Yoshioka, H., Watanabe, A., Dunn, J.C., Minas, T., 2011. Preoperative measurement of cartilage defects by MRI underestimates lesion size. Cartilage 2, 389–393.

Haralick, R.M., 1984. Digital step edges from zero crossing of second directional derivatives. IEEE Trans. Pattern Anal. Mach. Intell. 6, 58–68.

Heir, S., Nerhus, T.K., Røtterud, J.H., Loken, S., Ekeland, A., Engebretsen, L., Aroen, A., 2010. Focal cartilage defects in the knee impair quality of life as much as severe osteoarthritis. Am. J. Sports Med. 38, 231–237, http://dx.doi.org/10.1177/0363546509352157.

Hjelle, K., Solheim, E., Strand, T., Muri, R., Brittberg, M., 2002. Articular cartilage defects in 1,000 knee arthroscopies. Arthroscopy 18, 730–734.

Johnson, V.L., Hunter, D.J., 2014. The epidemiology of osteoarthritis. Best Pract. Res. Clin. Rheumatol. 28, 5–15, http://dx.doi.org/10.1016/j.berh.2014.01.004.

Kijowski, R., Blankenbaker, D.G., Stanton, P.T., Fine, J.P., De Smet, A.A., 2006. Radiographic findings of osteoarthritis versus arthroscopic findings of articular cartilage degeneration in the tibiofemoral joint. Radiology 239, 818–824, http://dx.doi.org/10.1148/radiol.2393050584.

Kladny, B., Bail, H., Swoboda, B., Schiwy-Bochat, H., Beyer, W.F., Weseloh, G., 1996. Cartilage thickness measurement in magnetic resonance imaging. Osteoarthritis Cartilage 4, 181–186, http://dx.doi.org/10.1016/S1063-4584(96)80014-8.

Li, X., Martin, S., Pitris, C., Ghanta, R., Stamper, D.L., Harman, M., Fujimoto, J.G., Brezinski, M.E., 2005. High-resolution optical coherence tomographic imaging of osteoarthritic cartilage during open knee surgery. Arthritis Res. Ther. 7, R318–R323, http://dx.doi.org/10.1186/ar1491 http://arthritis-research.com/content/7/2/R318.

Mayer, M.A., Borsdorf, A., Wagner, M., Hornegger, J., Mardin, C.Y., Tornow, R.P., 2012. Wavelet denoising of multiframe optical coherence tomography data. Biomed. Opt. Express 3, 572–589.

Messner, K., Maletius, W., 1996. The long-term prognosis for severe damage to weight-bearing cartilage in the knee: a 14-year clinical and radiographic follow-up in 28 young athletes. Acta Orthop. Scand. 67, 165–168.

Milentijevic, D., Rubel, I.F., Liew, A.S.L., Helfet, D.L., Torzilli, P.A., 2005. An in vivo rabbit model for cartilage trauma: a preliminary study of the influence of impact stress magnitude on chondrocyte death and matrix damage. J. Orthop. Trauma 19, 466–473.

Nebelung, S., Brill, N., Marx, U., Quack, V., Tingart, M., Schmitt, R., Rath, B., Jahr, H., 2015. Three-dimensional imaging and analysis of human cartilage degeneration using optical coherence tomography. J. Orthop. Res. 33, 651–659, http://dx.doi.org/10.1002/jor.22828.

Nebelung, S., Brill, N., Tingart, M., Pufe, T., Kuhl, C., Jahr, H., Truhn, D., 2016. Quantitative OCT and MRI biomarkers for the differentiation of cartilage degeneration. Skeletal Radiol. 45, 505–516, http://dx.doi.org/10.1007/s00256-016-2334-6.

Nebelung, S., Marx, U., Brill, N., Arbab, D., Quack, V., Jahr, H., Tingart, M., Zhou, B., Stoffel, M., Schmitt, R., Rath, B., 2014. Morphometric grading of osteoarthritis by optical coherence tomography—an ex vivo study. J. Orthop. Res. 32, 1381–1388, http://dx.doi.org/10.1002/jor.22673.

Oakley, S.P., Portek, I., Szomor, Z., Appleyard, R.C., Ghosh, P., Kirkham, B.W., Murrell, G.A.C., Lassere, M.N., 2005. Arthroscopy — a potential "gold standard" for the diagnosis of the chondropathy of early osteoarthritis. Osteoarthritis Cartilage 13, 368–378, http://dx.doi.org/10.1016/j.joca.2004.12.005.

Outerbridge, R.E., 1961. The etiology of chondromalacia patellae. J. Bone Joint Surg. Br. 43-B, 752–757.

Palmer, A.J.R., Brown, C.P., McNally, E.G., Price, A.J., Tracey, I., Jezzard, P., Carr, A.J., Glyn-Jones, S., 2013. Non-invasive imaging of cartilage in early osteoarthritis. Bone Joint J. 95-B, 738–746, http://dx.doi.org/10.1302/0301-620X.95B6.31414.

von Porat, A., 2004. High prevalence of osteoarthritis 14 years after an anterior cruciate ligament tear in male soccer players: a study of radiographic and patient relevant outcomes. Ann. Rheum. Dis. 63, 269–273, http://dx.doi.org/10.1136/ard.2003.008136.

Spahn, G., Klinger, H.M., Hofmann, G.O., 2009. How valid is the arthroscopic diagnosis of cartilage lesions? Results of an opinion survey among highly experienced arthroscopic surgeons. Arch. Orthop. Trauma. Surg. 129, 1117–1121, http://dx.doi.org/10.1007/s00402-009-0868-y.

Szczodry, M., Coyle, C.H., Kramer, S.J., Smolinski, P., Chu, C.R., 2009. Progressive chondrocyte death after impact injury indicates a need for chondroprotective therapy. Am. J. Sports Med. 37, 2318–2322, http://dx.doi.org/10.1177/0363546509348840.

Thompson, R.C.J., Oegema, T.R.J., Lewis, J.L., Wallace, L., 1991. Osteoarthrotic changes after acute transarticular load. An animal model. J. Bone Joint Surg. Am. 73, 990–1001.

Verteramo, A., Seedhom, B.B., 2007. Effect of a single impact loading on the structure and mechanical properties of articular cartilage. J. Biomech. 40, 3580–3589.

Wade, C.G., Šibalić, N., de Melo, N.R., Kondo, J.M., Adams, C.S., Weatherill, K.J., 2016. Real-time near-field terahertz imaging with atomic optical fluorescence. Nat. Photonics 11, 40–43, http://dx.doi.org/10.1038/nphoton.2016.214.

Winalski, C.S., Rajiah, P., 2011. The evolution of articular cartilage imaging and its impact on clinical practice. Skeletal Radiol. 40, 1197–1222, http://dx.doi.org/10.1007/s00256-011-1226-z.

Xie, T., Guo, S., Zhang, J., Chen, Z., Peavy, G.M., 2006. Determination of characteristics of degenerative joint disease using optical coherence tomography and polarization sensitive optical coherence tomography. Lasers Surg. Med. 38, 852–865, http://dx.doi.org/10.1002/lsm.20394.